Meccanica (2008) 43: 391–410
DOI 10.1007/s11012-007-9102-6

Computational modeling of biomagnetic micropolar blood flow and heat transfer in a two-dimensional non-Darcian porous medium

O. Anwar Bég · R. Bhargava · S. Rawat · Kalim Halim · H.S. Takhar

Received: 4 September 2006 / Accepted: 5 July 2007 / Published online: 18 December 2007

Abstract We study theoretically and computationally the incompressible, non-conducting, micropolar, biomagnetic (blood) flow and heat transfer through a two-dimensional square porous medium in an (x, y) coordinate system, bound by impermeable walls. The magnetic field acting on the fluid is generated by an electrical current flowing normal to the x–y plane, at a distance l beneath the base side of the square. The flow regime is affected by the magnetization B_0 and a linear relation is used to define the relationship between magnetization and magnetic field intensity. The steady governing equations for x-direction translational (linear) momentum, y-direction translational (linear) momentum, angular momentum (micro-rotation) and energy (heat) conservation are presented. The energy equation incorporates a special term designating the thermal power per unit volume due to the magnetocaloric effect. The governing equations are non-dimensionalized into a dimensionless (ξ, η) coordinate system using a set of similarity transformations. The resulting two point boundary value problem is shown to be represented by five dependent non-dimensional variables, f_ξ (velocity), f_η (velocity), g (micro-rotation), E (magnetic field intensity) and θ (temperature) with appropriate boundary conditions at the walls. The thermophysical parameters controlling the flow are the micropolar parameter (R), biomagnetic parameter (N_H), Darcy number (Da), Forchheimer (Fs), magnetic field strength parameter (Mn), Eckert number (Ec) and Prandtl number (Pr). Numerical solutions are obtained using the finite element method and also the finite difference method for $Ec = 2.476 \times 10^{-6}$ and Prandtl number $Pr = 20$,

Dedicated to Professor Y.C. Fung (1919-), Emeritus Professor of Biomechanics, Bioengineering Department, University of California at San Diego, USA for his seminal contributions to biomechanics and physiological fluid mechanics over four decades and his excellent encouragement to the authors, in particular OAB, with computational biofluid dynamics research.

O.A. Bég (✉)
Aerodynamics, Aerosciences Program, BAE Systems, King Faisal Air Academy, Riyadh, Saudi Arabia
e-mail: docoabeg@hotmail.com

R. Bhargava · S. Rawat
Applied Mathematic Group, Department of Mathematics, Indian Institute of Technology, Roorkee, India

R. Bhargava
e-mail: rbharfma@iitr.ernet.in

K. Halim
14 Brayston Gardens, Gatley, Cheadle, UK
e-mail: khalim@hotmail.co.uk

H.S. Takhar
Engineering Department, Manchester Metropolitan University, Oxford Rd., Manchester M15GD, UK
e-mail: h.s.takhar@mmu.ac.uk

Present address:
O.A. Bég
Engovation Engineering Science Research, 15 Southmere Avenue, Bradford BD73NU, UK

which represent realistic biomagnetic hemodynamic and heat transfer scenarios. Temperatures are shown to be considerably increased with Mn values but depressed by a rise in biomagnetic parameter (N_H) and also a rise in micropolarity (R). Translational velocity components are found to decrease substantially with micropolarity (R), a trend consistent with Newtonian blood flows. Micro-rotation values are shown to increase considerably with a rise in R values but are reduced with a rise in biomagnetic parameter (N_H). Both translational velocities are boosted with a rise in Darcy number as is micro-rotation. Forchheimer number is also shown to decrease translational velocities but increase micro-rotation. Excellent agreement is demonstrated between both numerical solutions. The mathematical model finds applications in blood flow control devices, hemodynamics in porous biomaterials and also biomagnetic flows in highly perfused skeletal tissue.

Keywords Biomagnetic · Micropolar · Heat transfer · Porous · Non-Darcian · Magnetization · Numerical · Mechanics of fluids · Prandtl number

Abbreviations

x, y	coordinates parallele and perpendicular to base of square in Fig. 1
u, v	x-direction and y-direction translational velocities
κ	vortex viscosity of biomagnetic, micropolar fluid
k^*	permeability of isotropic porous medium
b^*	Forchheimer inertial (quadratic drag) coefficient
ρ	density of biomagnetic, micropolar fluid
N	micro-rotation component (angular velocity of micro-elements)
T	temperature
ν	kinematic viscosity
μ_0	magnetic property
γ	micropolar spin-gradient viscosity (gyro-viscosity)
j	micro-inertia density
c_ρ	specific heat capacity of biomagnetic, micropolar fluid
k_f	thermal conductivity of biomagnetic, micropolar fluid
E^*	magnetic field intensity
T_c	Curie temperature of biomagnetic, micropolar fluid
Da	Darcy number
Fs	Forchheimer number
N_H	biomagnetic parameter
R	dimensionless micropolar vortex viscosity ratio
Rl	dimensionless micro-inertia density parameter
Mn	magnetization numberf
ε	dimensionless temperature ratio
Ec	Eckert (viscous dissipation) number
Pr	Prandtl number

1 Introduction

Mathematical modeling of heat transfer in biomedical engineering was initiated in the late 1940s in a seminal paper by Pennes [1] which laid the foundations for conduction heat transfer in tissue and introduced the celebrated bioheat transfer equation. Subsequently the field has expanded rapidly to embrace convection flows in hemodynamics and also radiative heat transfer in thermal ablation biotechnologies. Excellent reviews of progress in theoretical and numerical modeling of bio-heat transfer have been presented by Charny [2] and more recently by Rubinsky [3]. Research into convection heat transfer in blood flow in arteries and other physiological systems has been active since the late 1960s. Charm et al. [4] derived engineering heat transfer relations for convective blood flow. Victor and Shah [5] computed heat transfer rates for uniform heat flux and also uniform wall temperature cases in fully developed steady tube blood flows. They extended [6] this study to consider entrance effects. Further studies have been communicated by Chato [7], Lagendijk [8], Bég and Sajid [9], Craciiunescu and Clegg [10], Craciiunescu [11], Kolios et al. [12], Chakravarty and Sen [13], Baish [14], Deng and Liu [15], Craciiunescu and Clegg [16], Consiglieri et al. [17], Davalos et al. [18], Shrivastava et al. [19] and Gafiychuk et al. [20]. These studies were all confined to Newtonian blood flow models. However it has long been recognized that at low shear rates and in narrow blood vessels, the flow is generally strongly non-Newtonian. Many studies investigating various aspects of rheological blood flows have therefore appeared studying viscoelasticity of cells, hematocrit influence on rheological properties, shear-thinning and also micro-rotational effects. An excellent summary of a number of rheological models for blood was provided by Cokelet [21]. Skalak and Chien [22] presented an excellent examination of the non-Newtonian flow of blood, considering erthrocytes

as soft tissues. Further biorheological blood flow studies include those by Secomb et al. [23], Rodkiewicz et al. [24], Quemada [25] (who utilized a Maxwell viscoelastic model), Srivastava [26] who employed the couple-stress (polar) flow model to simulate stenotic blood flow, Anand and Rajagopal [27] who employed a generalized Oldroyd elasto-viscous model for steady and oscillatory blood flow and more recently Choi and Barakat [28] who used a shear-thinning Carreau fluid model. The rheological models considered above do not incorporate micro-structural effects i.e. they cannot simulate rotary motions and also gyration of fluid micro-elements which characterize suspensions in blood e.g. erythrocytes. Eringen [29] therefore formulated the *micropolar* fluid model to simulate such effects and subsequently many researchers have applied micropolar rheological theory to simulate blood flow in many scenarios. Ariman et al. [30] studied analytically the steady pulsating blood flow using a micropolar model, deriving solutions for the cell-rotation i.e. angular velocity and demonstrating this to be consistent with previous experimental findings. The micropolar theory was therefore shown to be able to realistically estimate low hematocrit blood flows in large conduits (radius $>$ 80 microns). It was also shown that the model could satisfactorily simulate blood flows at *any* hematocrit in *smaller* conduits. A rigorous discussion of the applicability of micropolar theory to hemodynamics was subsequently reported by Eringen and Kang [31]. Further micropolar blood flow studies have been communicated by Riha [32], Chaturani and Mahajan [33], Hogan and Henriksen [34], Muthu et al. [35], Atefi and Moosaie [36] and Cimpean et al. [37], this latter analysis discussing flow in a wavy (sinusoidal) channel. These micropolar blood flow studies were restricted to *purely fluid* regimes. However many regimes in biomechanics are in fact porous such as the lungs, tissue, cartilage, bone etc. Brain tissue is also known to be porous as are capillary beds, tumors and also soft connective tissue. In cardiovascular flows also porous media transport is very important. Generally the Darcy law has been employed to simulate flows in porous bio-materials at low Reynolds numbers, for example flow in soft tissues, alveoli surface diffusion etc. However at higher velocities the flows are no longer viscous-dominated but inertially-dominated and extensions to the Darcy model are needed. The most popular is the Darcy-Forchheimer drag force model which incorporates a second order (quadratic) term which dominates impedance effects at higher Reynolds numbers, usually above 10. Several authors have employed porous drag force models in biofluid simulations. Significant works include those by Sorek and Sideman [38] who analyzed blood flow in cardiac vessels using a Darcy-Forchheimer model, Preziosi and Farina [39] who studied mass exchange using an extended Darcy model, Vankan et al. [40] who considered non-Darcy transport in blood-perfused tissue and Axtell et al. [41] who discussed blood circulation in tissues as a multiscale, multiphase porous media problem by simulating the fluid phase as a micromorphic continuum. While blood is known to be Newtonian, it also has electrically-conducting properties. The presence of iron oxides in the haemoglobin molecule has been shown [42] to produce strong magnetic properties in blood. Under oxygenated conditions blood exhibits diamagnetic properties and under deoxygenated conditions it behaves as a paramagnetic fluid. Several researchers have therefore studied magneto-hemodynamic flows over the past few decades, including Sud et al. [43] for MHD pumping of blood and Wagh and Wagh [44] who studied numerically the hydromagnetic blood flow in conduits indicating that the magnetic body force retards flow velocities. A more rigorous study of biomagnetic blood flow utilizing *ferrohydrodynamics* was presented by Haik et al. [45]. Sud and Sekhon [46] studied the magneto-hemodynamic blood flow via a network of rigid tubes using a finite element method. Several authors have also reported on heat transfer in biomagnetofluid flows including Tzirtzilakis and Tanoudis [47] for biomagnetic convective heat transfer over a stretching surface and Louckopoulos and Tzirtzilakis [48] for biomagnetic flow and heat transfer in a parallel-plate system. Bhargava et al. [49] recently presented the first mathematical model for biomagnetic flow of a micropolar fluid in a porous medium using finite element analysis. We note also that several important isothermal and non-isothermal biomagnetic flow models have been developed. Haik et al. [50] have presented a robust model for biomagnetic flow dynamics. Tzirtzilakis [51] has extended the model of Haik et al. [50] by considering large electrical conductivity of the blood and non-isothermal behavior in the energy equation formulation. This study however concerned Newtonian blood flow. Thusfar however the *isothermal* biomagnetic heat transfer in a *micropolar-fluid* saturated non-Darcian porous medium has not been inves-

tigated despite important applications in hemodynamics and physiological flow control devices. The present study therefore while isothermal extends the current literature in three principal areas- the simulation of transport of the biomagnetic fluid in porous media, micropolar characteristics of the fluid and also with a finite element solution methodology. We have as with the earlier studies [49] utilized a simple geometry and an elementary porous medium drag force model. Our objective is to study the general influence of biomagnetism, micropolarity, magnetic field strength and the porous impedances on the flow and heat transfer in the porous regime.

2 Mathematical model

Consider the laminar, viscous, incompressible, non-conducting, micropolar, biomagnetic blood flow and heat transfer through a square-shaped two-dimensional (x, y) porous medium bound by impermeable walls, as illustrated in Fig. 1. The square regime has dimensions $L \times L$ and the x, y axes intersect at the bottom left corner of the square with coordinates $(0, 0)$. A magnetic field acting on the fluid is produced by an electrical current flowing normal to the x–y plane, at a distance l beneath the base side of the square. The flow regime is affected by the magnetization B_0 and following Tzirtzilakis and Tanoudis [47], a linear relation is used to define the relationship between magnetization and magnetic field intensity, E^* as follows:

$$B_0 = J E^*, \tag{1}$$

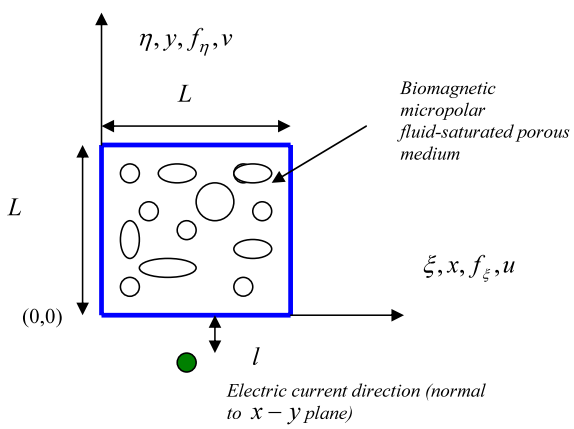

Fig. 1 Physical model and coordinate system

where E^* is the magnetic field intensity and J is a constant. The magnetic field applied is of adequate magnitude to saturate the biomagnetic fluid. The porous medium is modeled using a Darcy-Forcheimmer drag-force formulation, following Bég et al. [49]. Using the analogy to ferrohydrodynamic flows, the biomagnetic fluid model of Tzirtzilakis [51] shows that since the magnetic field used is that of a dipole and thereby for sufficiently sharp magnetic field gradient, the electrical conductivity of blood can be neglected. Also [51] indicates that for low velocity flows (as encountered in porous media transport), the Lorentz force generated by the electrical conductivity of the blood can be neglected. We have extended the analysis of [51] with the micropolar fluid theory herein but considered only the isothermal case. The micropolar biomagnetic flow and convection heat transfer in a two-dimensional Darcy-Forcheimmer porous medium, with zero-pressure gradient can then be shown to be described by the following conservation equations:

$$\frac{\partial u}{\partial x} + \frac{\partial \upsilon}{\partial y} = 0, \tag{2}$$

$$u\frac{\partial u}{\partial x} + \upsilon\frac{\partial u}{\partial y} = \left(\upsilon + \frac{\kappa}{\rho}\right)\left(\frac{\partial^2 u}{\partial x^2} + \frac{\partial^2 u}{\partial y^2}\right) + \frac{\mu_0 B_0}{\rho}\frac{\partial E^*}{\partial x} - \frac{\upsilon u}{k^*} - \frac{b^* u}{k^*} + \frac{\kappa}{\rho}\left(\frac{\partial N}{\partial x} + \frac{\partial N}{\partial y}\right), \tag{3}$$

$$u\frac{\partial \upsilon}{\partial x} + \upsilon\frac{\partial \upsilon}{\partial y} = \left(\upsilon + \frac{\kappa}{\rho}\right)\left(\frac{\partial^2 \upsilon}{\partial x} + \frac{\partial^2 \upsilon}{\partial y^2}\right) + \frac{\mu_0 B_0}{\rho}\frac{\partial E^*}{\partial y} - \frac{\upsilon \upsilon}{k^*} - \frac{b^* \upsilon}{k^*} + \frac{\kappa}{\rho}\left(\frac{\partial N}{\partial x} + \frac{\partial N}{\partial y}\right), \tag{4}$$

$$u\frac{\partial N}{\partial x} + \upsilon\frac{\partial N}{\partial y} = -\frac{\kappa}{\rho j}\left(2N + \frac{\partial u}{\partial x} + \frac{\partial \upsilon}{\partial y}\right) + \frac{\gamma}{\rho j}\left(\frac{\partial^2 N}{\partial x^2} + \frac{\partial^2 N}{\partial y^2}\right), \tag{5}$$

$$\rho c_p\left(u\frac{\partial T}{\partial x} + \upsilon\frac{\partial T}{\partial y}\right) + \mu_0 T\frac{\partial B_0}{\partial T}\left(u\frac{\partial E^*}{\partial x} + \upsilon\frac{\partial E^*}{\partial y}\right) = k_f\left(\frac{\partial^2 T}{\partial x^2} + \frac{\partial^2 T}{\partial y^2}\right), \tag{6}$$

where all terms are defined in the nomenclature, at the end of the paper. In the x and y momentum conservation equations, (3) and (4) separate Darcian porous body force terms, are present, $-\frac{vu}{k*}, -\frac{v\upsilon}{k*}$ respectively and also separate Forcheimmer second order drag force terms, $-\frac{b*u^2}{k*}$ and $-\frac{b*\upsilon^2}{k*}$. In (3), the term $\frac{\mu_o B_0}{\rho}\frac{\partial E^*}{\partial x}$ denotes the magnetic force per unit mass along the x-axis and in (4) $\frac{\mu_o B_0}{\rho}\frac{\partial E^*}{\partial y}$ designates the magnetic force per unit mass along the y-axis. The term $\mu_0 T\frac{\partial B_0}{\partial T}(u\frac{\partial E}{\partial x}+v\frac{\partial E}{\partial y})$ of (6) represents the thermal power per unit volume due to the magnetocaloric effect [51]. In the present formulation, as well as in that of biomagnetic fluid density, the blood is actually considered as electrically nonconducting magnetic fluid. Thus, for variation of magnetization, with the magnetic field intensity and temperature, the following relation, derived experimentally for a magnetic fluid by Matsuki et al. [52], is considered. This equation has also been utilized in the models described in [47] and [48].

$$B_0 = K^* E^* (T_c - T). \tag{7}$$

Following Tzirtzilakis and Tanoudis [47], magnetization B_0 is assumed to be a function of magnetic field intensity E^*. The magnitude of the latter at any point in the square medium (x, y) is given by [50]:

$$E^*(x,y) = \frac{\gamma^*}{2\pi}\left[\frac{1}{(x-\frac{L}{2})^2+(y-l)^2}\right], \tag{8}$$

where γ^* denotes the magnetic field strength at $x = L/2$, $y = -l$ i.e. at the point in Fig. 1, where electric current is flowing, distance l beneath the centre point of the base of the square medium. The appropriate boundary conditions for the problem are given by:

$$\begin{aligned} &x=0, \qquad u=0, \qquad \upsilon=0,\\ &N=0.5\frac{\partial \upsilon}{\partial x}, \qquad \frac{\partial T}{\partial x}=0, \end{aligned} \tag{9a}$$

$$\begin{aligned} &x=1, \qquad u=0, \qquad \upsilon=0,\\ &N=0.5\frac{\partial \upsilon}{\partial x}, \qquad \frac{\partial T}{\partial x}=0, \end{aligned} \tag{9b}$$

$$\begin{aligned} &y=0, \qquad u=0, \qquad \upsilon=0,\\ &N=-0.5\frac{\partial u}{\partial y}, \qquad T=T_u, \end{aligned} \tag{9c}$$

$$\begin{aligned} &y=1, \qquad u=0, \qquad \upsilon=0,\\ &N=-0.5\frac{\partial u}{\partial y}, \qquad T=T_1. \end{aligned} \tag{9d}$$

3 Transformation of model

Introducing the dimensionless function $f(\eta)$ and $g(\eta)$ such that the continuity equation is automatically satisfied and taking the similarity transformation:

$$\begin{aligned} &\xi=\frac{x}{L}, \qquad \eta=\frac{y}{L}, \qquad f_\xi=\frac{uL}{v}, \qquad f_\eta=\frac{\upsilon L}{v},\\ &g=\frac{NL^2}{v}, \qquad \gamma=\left[\mu+\frac{\kappa}{2}\right]j,\\ &E=\frac{E^*}{E_0^*}, \qquad \theta=\frac{T_u-T}{T_u-T_1}, \end{aligned} \tag{10}$$

where E_0^* is the magnetic field intensity at the point $(L/2, 0)$:

$$E_0^* = \frac{\gamma^*}{2\pi}\left[\frac{1}{(\frac{L}{2}-\frac{L}{2})^2+(0-l)^2}\right] = \frac{\gamma^*}{2\pi l^2}, \tag{11}$$

$$\begin{aligned} E &= \frac{E*}{E_o*} = \frac{2\pi l^2}{\gamma^*}\frac{\gamma^*}{2\pi}\left[\frac{1}{(x-\frac{L}{2})^2+(y-l)^2}\right]\\ &= \frac{l^2}{(\xi L-\frac{L}{2})^2+(\eta L-l)^2}. \end{aligned} \tag{12}$$

The governing equations (3) to (6) then reduce to the following set of differential equations:

$$\begin{aligned} &f_\xi\frac{\partial f_\xi}{\partial \xi}+f_\eta\frac{\partial f_\xi}{\partial \eta}\\ &\quad=(1+R)\left(\frac{\partial^2 f_\xi}{\partial \xi^2}+\frac{\partial^2 f_\xi}{\partial \eta^2}\right)+N_H\frac{\partial E}{\partial \xi}-\frac{f_\xi}{Da}\\ &\qquad-\frac{Fsf_\xi^2}{Da^2}+R\left(\frac{\partial g}{\partial \xi}+\frac{\partial g}{\partial \eta}\right), \end{aligned} \tag{13}$$

$$\begin{aligned} &f_\xi\frac{\partial f_\eta}{\partial \xi}+f_\eta\frac{\partial f_\eta}{\partial \eta}\\ &\quad=(1+R)\left(\frac{\partial^2 f_\eta}{\partial \xi^2}+\frac{\partial^2 f_\eta}{\partial \eta^2}\right)+N_H\frac{\partial E}{\partial \xi}-\frac{f_\eta}{Da}\\ &\qquad-\frac{Fsf_\eta^2}{Da^2}+R\left(\frac{\partial g}{\partial \xi}+\frac{\partial g}{\partial \eta}\right), \end{aligned} \tag{14}$$

$$f_\xi \frac{\partial g}{\partial \xi} + f_\eta \frac{\partial g}{\partial \eta} = -R_1 R\left(2g + \frac{\partial f_\xi}{\partial \xi} + \frac{\partial f_\eta}{\partial \eta}\right) + \left(1 + \frac{R}{2}\right)\left(\frac{\partial^2 g}{\partial \xi^2} + \frac{\partial^2 g}{\partial \eta^2}\right), \quad (15)$$

$$\nabla^2 \theta = Pr\left(f_\xi \frac{\partial \theta}{\partial \xi} + f_\eta \frac{\partial \theta}{\partial \eta}\right) + Mn\,Ec\,Pr\,E(\theta - \varepsilon)\left(f_\xi \frac{\partial E}{\partial \xi} + f_\eta \frac{\partial E}{\partial \eta}\right), \quad (16)$$

where

$$Da = \frac{k*}{L^2}, \qquad Fs = \frac{b*}{L}, \qquad N_H = \frac{L^2 \mu_o k^* E_0^2}{v^2 \rho},$$

$$R = \frac{\kappa}{\mu}, \qquad R_1 = \frac{L^2}{j},$$

$$Mn = \frac{\mu_0 E_0^2 K^* (T_u - T_1)}{\rho u^2}, \qquad \varepsilon = \frac{T_u}{(T_u - T_1)},$$

$$Ec = \frac{u^2}{c_p (T_u - T_1)}, \qquad Pr = \frac{c_p \mu}{k_f}.$$

The corresponding boundary conditions also transform to:

$$\xi = 0, \quad f_\xi = 0, \quad f_\eta = 0, \quad g = 0.5\frac{\partial f_\eta}{\partial \xi}, \quad \frac{\partial \theta}{\partial \xi} = 0, \quad (17a)$$

$$\xi = 1, \quad f_\xi = 0, \quad f_\eta = 0, \quad \mathrm{g} = 0.5\frac{\partial f_\eta}{\partial \xi}, \quad \frac{\partial \theta}{\partial \xi} = 0, \quad (17b)$$

$$\eta = 0, \quad f_\xi = 0, \quad f_\eta = 0, \quad \mathrm{g} = -0.5\frac{\partial f_\xi}{\partial \eta}, \quad \theta = 0, \quad (17c)$$

$$\eta = 1, \quad f_\xi = 0, \quad f_\eta = 0, \quad \mathrm{g} = -0.5\frac{\partial f_\xi}{\partial \eta}, \quad \theta = 1. \quad (17d)$$

We note that the parameter, Mn, appears in a number of biomagnetic fluid dynamics studies and has been derived in the analysis presented in [48] and also in the models by Tzirtzilakis and Tanoudis [47] in the context of stretching sheet flow. With regard to the micro-rotation boundary condition in (17c) regarding the rotary motions of micro-elements at the wall, several alternative versions of this condition have been used. While it is apparent that the magnetic field close to the boundary ($\eta = 0$) is strong and the rotational movements of the micro-elements of the biomagnetic micropolar fluid (blood) i.e. corpuscles will be drastically reduced due to equilibrium magnetization, they will not necessarily vanish completely. While the argument for zero spin at the wall is justified to some extent (microelements are physically incapable of rotating at the wall), however Ahmadi [55] has shown rigorously that the wall gradient of the gyration vector must approach zero at the wall. This approach has been adopted by many studies where greater accuracy is needed at the wall. For example Dey and Nath [56] have employed this approach, which incidentally is more consistent with the framework of boundary layer growth at the wall, then the simple reduction to a vanishing micro-rotation boundary condition. Of course micro-element rotary motions will be inhibited at the wall but not necessarily totally eliminated; the rate of change of micro-rotation will be zero owing to arguments from thermodynamics as described by Ahmadi [55]. Of interest in engineering applications are the average value of Nusselt number on the horizontal wall, which is defined by:

$$Nu = \int_0^1 \left(\frac{\partial \theta}{\partial \eta}\right)_{\eta=1} d\xi. \quad (18)$$

4 Numerical solutions

Computational solutions to the transformed model have been obtained using the finite element method and also the finite difference method. We shall discuss now briefly the numerical formulations for both methods.

4.1 Finite element method

4.1.1 Variational formulation

The variational form associated with equations (13) to (16) over a typical square element is given by:

$$\int_{\Omega^e} w_1\Big(f_\xi\frac{\partial f_\xi}{\partial\xi}+f_\eta\frac{\partial f_\xi}{\partial\eta}-(1+R)\Big(\frac{\partial^2 f_\xi}{\partial\xi^2}+\frac{\partial^2 f_\xi}{\partial\eta^2}\Big) - N_H\frac{\partial E}{\partial\xi}+\frac{f_\xi}{Da}+\frac{Fsf_\xi^2}{Da^2} - R\Big(\frac{\partial g}{\partial\xi}+\frac{\partial g}{\partial\eta}\Big)\Big)d\xi d\eta=0, \tag{19}$$

$$\int_{\Omega^e} w_2\Big(f_\xi\frac{\partial f_\eta}{\partial\xi}+f_\eta\frac{\partial f_\eta}{\partial\eta}-(1+R)\Big(\frac{\partial^2 f_\eta}{\partial\xi^2}+\frac{\partial^2 f_\eta}{\partial\eta^2}\Big) - N_H\frac{\partial E}{\partial\xi}+\frac{f_\eta}{Da}+\frac{Fsf_\eta^2}{Da^2} - R\Big(\frac{\partial g}{\partial\xi}+\frac{\partial g}{\partial\eta}\Big)\Big)d\xi d\eta=0, \tag{20}$$

$$\int_{\Omega^e} w_3\Big(f_\xi\frac{\partial g}{\partial\xi}+f_\eta\frac{\partial g}{\partial\eta}-R_1R\Big(2g+\frac{\partial f_\xi}{\partial\xi}+\frac{\partial f_\eta}{\partial\eta}\Big) +\Big(1+\frac{R}{2}\Big)\Big(\frac{\partial^2 g}{\partial\xi^2}+\frac{\partial^2 g}{\partial\eta^2}\Big)\Big)d\xi d\eta=0, \tag{21}$$

$$\int_{\Omega^e} w_4\Big(\nabla^2\theta-Pr\Big(f_\xi\frac{\partial\theta}{\partial\xi}+f_\eta\frac{\partial\theta}{\partial\eta}\Big) - MnEcPrE(\theta-\varepsilon)\Big(f_\xi\frac{\partial E}{\partial\xi}+f_\eta\frac{\partial E}{\partial\eta}\Big)\Big)d\xi d\eta=0, \tag{22}$$

where w_1, w_2, w_3 and w_4 are arbitrary test functions and may be viewed as the variation in f_ξ, f_η, g and θ respectively.

$$\int_{\Omega^e} w_1\Big(\overline{f_\xi}\frac{\partial f_\xi}{\partial\xi}+\overline{f_\eta}\frac{\partial f_\xi}{\partial\eta}\Big)d\xi d\eta - (1+R)\int_{\Omega^e}\frac{\partial w_1}{\partial\xi}\Big(\frac{\partial f_\xi}{\partial\xi}+\frac{\partial f_\xi}{\partial\eta}\Big)d\xi d\eta - \int_{\Omega_e} w_1N_H\frac{\partial E}{\partial\xi}d\xi d\eta + \int_{\Omega_e} w_1\frac{f_\xi}{Da}d\xi d\eta+\frac{Fs}{Da^2}\int_{\Omega^e} w_1f_\xi\overline{f_\xi}d\xi d\eta - R\int_{\Omega_e} w_1\Big(\frac{\partial g}{\partial\xi}+\frac{\partial g}{\partial\eta}\Big)d\xi d\eta=\oint wq_{n1}ds, \tag{23}$$

$$q_{n_1}=-\Big(n_\xi\frac{\partial f_\xi}{\partial\xi}+n_\eta\frac{\partial f_\eta}{\partial\eta}\Big), \tag{24}$$

$$\int_{\Omega^e} w_1\Big(\overline{f_\xi}\frac{\partial f_\xi}{\partial\xi}+\overline{f_\eta}\frac{\partial f_\xi}{\partial\eta}\Big)d\xi d\eta - (1+R)\int_{\Omega^e}\frac{\partial w_1}{\partial\xi}\Big(\frac{\partial f_\xi}{\partial\xi}+\frac{\partial f_\xi}{\partial\eta}\Big)d\xi d\eta - \int_{\Omega_e} w_1N_H\frac{\partial E}{\partial\xi}d\xi d\eta + \int_{\Omega_e} w_1\frac{f_\eta}{Da}d\xi d\eta+\frac{Fs}{Da^2}\int_{\Omega^e} w_1f_\eta\overline{f_\eta}d\xi d\eta - R\int_{\Omega_e} w_1\Big(\frac{\partial g}{\partial\xi}+\frac{\partial g}{\partial\eta}\Big)d\xi d\eta=\oint wq_{n2}ds, \tag{25}$$

$$q_{n_2}=-\Big(n_\xi\frac{\partial f_\xi}{\partial\xi}+n_\eta\frac{\partial f_\eta}{\partial\eta}\Big), \tag{26}$$

$$\int_{\Omega_e} w_3\Big(\overline{f_\xi}\frac{\partial g}{\partial\xi}+\overline{f_\eta}\frac{\partial g}{\partial\eta}\Big)d\xi d\eta - R_1R\int_{\Omega_e} w_1\Big(2g+\frac{\partial f_\xi}{\partial\xi}+\frac{\partial f_\eta}{\partial\eta}\Big)d\xi d\eta+\Big(1+\frac{R}{2}\Big)\int_{\Omega_e} w_1\Big(\frac{\partial g}{\partial\xi}+\frac{\partial g}{\partial\eta}\Big)d\xi d\eta =\oint wq_{n3}ds, \tag{27}$$

$$q_{n3}=-\Big(n_\xi\frac{\partial g_\xi}{\partial\xi}+n_\eta\frac{\partial g_\eta}{\partial\eta}\Big) \tag{28}$$

$$\int_{\Omega^e} w_4\Big(\frac{\partial^2\theta}{\partial\xi^2}+\frac{\partial^2\theta}{\partial\eta^2}\Big)d\xi d\eta - Pr\int_{\Omega^e} w_4\Big(f_\xi\frac{\partial\theta}{\partial\xi}+f_\eta\frac{\partial\theta}{\partial\eta}\Big)d\xi d\eta - MnEcPr\int_{\Omega^e} w_4E(\theta-\varepsilon)\times\Big(f_\xi\frac{\partial E}{\partial\xi}+f_\eta\frac{\partial E}{\partial\eta}\Big)d\xi d\eta =\oint wq_{n4}ds, \tag{29}$$

$$q_{n4}=-\Big(n_\xi\frac{\partial\theta_\xi}{\partial\xi}+n_\eta\frac{\partial\theta_\eta}{\partial\eta}\Big). \tag{30}$$

From an inspection of the boundary term in the above equations, it is found that the specification of the function constitutes the essential boundary condition, and hence these functions are the primary variables. The specification of the coefficient of the weight functions in the boundary expression constitutes the nat-

ural boundary condition: Here q'_{ni}s are the secondary variables of the formulation.

4.1.2 Shape functions

Triangular, rectangular as well as square element can be chosen according to the shape of the domain. Here square elements with linear interpolation functions are used because they are more appropriate than the triangular or rectangular elements. Details of the description of elements are available in Reddy [57]. In the present computations ψ_1, ψ_2, ψ_3 and ψ_4 are taken as linear interpolation functions for a square element Ω^e which are excluded here for brevity.

4.1.3 Finite element formulation

The structure domain defined as: $0 \leq \xi \leq 1$ and $0 \leq \eta \leq 1$ is discretized into square elements of same size using the finite element approximations:

$$\begin{aligned} f_\xi &= \sum_{j=1}^{n} f_{\xi j}\psi_j(\xi,\eta), \qquad f_\eta = \sum_{j=1}^{n} f_{\eta j}\psi_j(\xi,\eta), \\ g &= \sum_{j=1}^{n} g_j\psi_j(\xi,\eta), \qquad \theta = \sum_{j=1}^{n} \theta_j\psi_j(\xi,\eta), \end{aligned} \tag{31}$$

where $n = 3, 4, 6$ and 8 is for linear triangular element, linear rectangular element, quadratic triangular element and quadratic rectangular element respectively. Effectively the finite element model of the equations thus formed is given by:

$$\begin{bmatrix} [K^{11}] & [K^{12}] & [K^{13}] & [K^{14}] & [K^{15}] & [K^{16}] \\ [K^{21}] & [K^{22}] & [K^{23}] & [K^{24}] & [K^{25}] & [K^{26}] \\ [K^{31}] & [K^{32}] & [K^{33}] & [K^{34}] & [K^{35}] & [K^{36}] \\ [K^{41}] & [K^{42}] & [K^{43}] & [K^{44}] & [K^{45}] & [K^{46}] \\ [K^{51}] & [K^{52}] & [K^{53}] & [K^{54}] & [K^{55}] & [K^{56}] \\ [K^{61}] & [K^{62}] & [K^{63}] & [K^{64}] & [K^{65}] & [K^{66}] \end{bmatrix} \times \begin{bmatrix} \{f_\xi\} \\ \{f_\eta\} \\ \{\psi\} \\ \{\theta\} \\ \{\phi\} \\ \{g\} \end{bmatrix} = \begin{bmatrix} \{r^1\} \\ \{r^2\} \\ \{r^3\} \\ \{r^4\} \\ \{r^5\} \\ \{r^6\} \end{bmatrix}, \tag{32}$$

$$[K^{11}] = \begin{bmatrix} K_{11}^{11} & K_{12}^{11} & K_{13}^{11} & K_{14}^{11} \\ K_{21}^{11} & K_{22}^{11} & K_{23}^{11} & K_{24}^{11} \\ K_{31}^{11} & K_{32}^{11} & K_{33}^{11} & K_{34}^{11} \\ K_{41}^{11} & K_{42}^{11} & K_{43}^{11} & K_{44}^{11} \end{bmatrix}, \tag{33}$$

$$\{f_\xi\} = \begin{Bmatrix} f_{\xi 1} \\ f_{\xi 2} \\ f_{\xi 3} \\ f_{\xi 4} \end{Bmatrix}, \qquad \{r^1\} = \begin{Bmatrix} r_1^1 \\ r_2^1 \\ r_3^1 \\ r_4^1 \end{Bmatrix},$$

where

$$\overline{f_\xi} = \sum_{i=1}^{4} \psi_i f_{\xi i}, \qquad \overline{f_\eta} = \sum_{i=1}^{4} \psi_i f_{\eta i}. \tag{34}$$

The whole domain is divided into 100 square elements of length 0.1. Each element is four nodded therefore whole domain contains 121 nodes. At each node 4 functions are to be evaluated hence after assembly of the element equations, we obtain a system of 484 equations which is non linear therefore an iterative scheme is used for solving it. The system is linearized by incorporating the functions $\overline{f_\xi}$ and $\overline{f_\eta}$, which are assumed to be known. The system of linear equations has been solved by using Gauss elimination method by maintaining an accuracy of 0.0005. It has been observed that in the same domain the accuracy is not effected even if the number of elements are increased by decreasing the size of the elements, else it increases the computational time only. The technique has been used extensively by the authors in many other thermofluid dynamics studies. For example Takhar et al. [58] used the finite element method to study the transient 3-dimensional micropolar stagnation point convection heat transfer. Bhargava et al. [59] analyzed the mixed convection micropolar flow stretching flow using finite elements. More recently Bég et al. [60] studied the third order viscoelastic hydromechanics in a non-Darcian porous medium with wall transpiration using the finite element method.

4.2 Finite difference method

For the comparison purpose the same system of equations (13) to (16), subject to boundary conditions (17) are solved numerically using the finite difference method. This technique is equally efficient for ordinary as well as partial differential equations in boundary value problems as well as initial value problems.

Implementing *central difference* formulae, the set of equations (13) to (16), can be written as:

$$f_{\xi i,j}\frac{(f_{\xi i+1,j}-f_{\xi i-1,j})}{2he}+f_{\eta i,i}\frac{(f_{\xi i,j+1}-f_{\xi i,j-1})}{2ke}$$
$$=(1+R)\left(\frac{(f_{\xi i+1,j}-2f_{\xi i,j}+f_{\xi i-1,j})}{he^2}\right.$$
$$\left.+\frac{(f_{\eta i,j+1}-2f_{\eta i,j}+f_{\eta i,j-1})}{ke^2}\right)$$
$$+N_H\left(\frac{E_{i+1,j}-E_{i-1,j}}{he}\right)-\frac{f_{\xi i,j}}{Da}-\frac{Fsf_{\xi i,j}^2}{Da^2}$$
$$+R\left(\frac{g_{i+1,j}-g_{i-1,j}}{2he}+\frac{g_{i,j+1}-g_{i,j-1}}{2ke}\right), \quad (35)$$

$$f_{\xi i,j}\frac{(f_{\eta i+1,j}-f_{\eta i-1,j})}{2he}+f_{\eta i,i}\frac{(f_{\eta i,j+1}-f_{\eta i,j-1})}{2ke}$$
$$=(1+R)\left(\frac{(f_{\eta i+1,j}-2f_{\eta i,j}+f_{\eta i-1,j})}{he^2}\right.$$
$$\left.+\frac{(f_{\eta i,j+1}-2f_{\eta i,j}+f_{\eta i,j-1})}{ke^2}\right)$$
$$+N_H\left(\frac{E_{i+1,j}-E_{i-1,j}}{2he}\right)-\frac{f_{\eta i,j}}{Da}-\frac{Fsf_{\eta i,j}^2}{Da^2}$$
$$+R\left(\frac{g_{i+1,j}-g_{i-1,j}}{2he}+\frac{g_{i,j+1}-g_{i,j-1}}{2ke}\right), \quad (36)$$

$$f_{\xi i,j}\frac{(g_{\eta i+1,j}-g_{\eta i-1,j})}{2he}+f_{\eta i,i}\frac{(g_{\eta i,j+1}-g_{\eta i,j-1})}{2ke}$$
$$=\left(1+\frac{R}{2}\right)\left(\frac{(g_{\eta i+1,j}-2g_{\eta i,j}+g_{\eta i-1,j})}{he^2}\right.$$
$$\left.+\frac{(g_{\eta i,j+1}-2g_{\eta i,j}+g_{\eta i,j-1})}{ke^2}\right)$$
$$-R_1R\left(2g_{i,j+1}\frac{f_{\xi i+1,j}-f_{\xi i-1,j}}{2he}\right.$$
$$\left.+\frac{f_{\xi i,j+1}-f_{\xi i,j-1}}{2ke}\right), \quad (37)$$

$$Pr\left(f_{\xi i,j}\frac{(\theta_{\eta i+1,j}-\theta_{\eta i-1,j})}{2he}\right.$$
$$\left.+f_{\eta i,i}\frac{(\theta_{\eta i,j+1}-\theta_{\eta i,j-1})}{2ke}\right)$$
$$+PrMnEcE_{i,j}(\theta_{i,j}-\varepsilon)$$
$$\times\left(f_{\xi i,j}\frac{(E_{i+1,j}-E_{i-1,j})}{2he}\right.$$
$$\left.+f_{\eta i,i}\frac{(E_{i,j+1}-E_{i,j-1})}{2ke}\right)$$
$$=\left(\frac{(\theta_{\eta i+1,j}-2\theta_{\eta i,j}+\theta_{\eta i-1,j})}{he^2}\right.$$
$$\left.+\frac{(\theta_{\eta i,j+1}-2\theta_{\eta i,j}+\theta_{\eta i,j-1})}{ke^2}\right), \quad (38)$$

where $i, j = 2, 3, \ldots, 10$; he and ke are the step length. Since the above equations are non-linear and coupled, hence analytical solutions are intractable. Therefore an iterative scheme is necessary. Casting the equations in the form:

$$x_i = F(l_1, l_2, \ldots, l_n), \quad (39)$$

where each l_i is the function of the variable f_ξ, f_η, g and θ, x_i is any of the variable f_ξ, f_η, g and θ. Now starting with initial guess values, new iterate values are obtained. This process continues till the absolute error $|x_i - x_{i-1}|$ is less than the accuracy required. The condition of convergence of the scheme is checked before implementing the iterative scheme.

5 Special cases of the flow model

We shall now discuss several pertinent special cases of the flow model. In all cases the mass conservation and energy conservation equations are unaffected, and only modifications to the f_ξ and f_η translational momentum equations are performed.

Case I: Purely hydrodynamic micropolar flow in a fluid regime

With $N_H = 0$, all magnetic effects disappear from the momentum equations (13) and (14). Also as $Da \to \infty$ and $Fs \to 0$, then the regime becomes purely fluid and Darcian and Forcheimmer drag forces disappear. The translational momentum equations now become:

$$f_\xi\frac{\partial f_\xi}{\partial \xi}+f_\eta\frac{\partial f_\xi}{\partial \eta}=(1+R)\left(\frac{\partial^2 f_\xi}{\partial \xi^2}+\frac{\partial^2 f_\xi}{\partial \eta^2}\right)$$
$$+R\left(\frac{\partial g}{\partial \xi}+\frac{\partial g}{\partial \eta}\right), \quad (40)$$

$$f_\xi \frac{\partial f_\eta}{\partial \xi} + f_\eta \frac{\partial f_\eta}{\partial \eta} = (1+R)\left(\frac{\partial^2 f_\eta}{\partial \xi^2} + \frac{\partial^2 f_\eta}{\partial \eta^2}\right) + R\left(\frac{\partial g}{\partial \xi} + \frac{\partial g}{\partial \eta}\right). \quad (41)$$

The microrotation (angular velocity) conservation equation and energy equations remains unchanged from (15) and (16), as do the general case boundary conditions (17).

Case II: Biomagnetic micropolar flow in a purely fluid regime

With $Da \to \infty$ and $Fs \to 0$, then the regime becomes purely fluid and Darcian and Forcheimmer drag forces disappear. The translational momentum equations now become for non-zero N_H:

$$f_\xi \frac{\partial f_\xi}{\partial \xi} + f_\eta \frac{\partial f_\xi}{\partial \eta} = (1+R)\left(\frac{\partial^2 f_\xi}{\partial \xi^2} + \frac{\partial^2 f_\xi}{\partial \eta^2}\right) + N_H \frac{\partial E}{\partial \xi} + R\left(\frac{\partial g}{\partial \xi} + \frac{\partial g}{\partial \eta}\right), \quad (42)$$

$$f_\xi \frac{\partial f_\eta}{\partial \xi} + f_\eta \frac{\partial f_\eta}{\partial \eta} = (1+R)\left(\frac{\partial^2 f_\eta}{\partial \xi^2} + \frac{\partial^2 f_\eta}{\partial \eta^2}\right) + N_H \frac{\partial E}{\partial \xi} + R\left(\frac{\partial g}{\partial \xi} + \frac{\partial g}{\partial \eta}\right). \quad (43)$$

Case III: Biomagnetic micropolar flow in a Darcian porous medium

With $Fs \to 0$ only Forcheimmer drag forces disappear i.e. the model is valid for creeping flows with only Darcian bulk matrix impedance. The momentum equations now become for non-zero N_H:

$$f_\xi \frac{\partial f_\xi}{\partial \xi} + f_\eta \frac{\partial f_\xi}{\partial \eta} = (1+R)\left(\frac{\partial^2 f_\xi}{\partial \xi^2} + \frac{\partial^2 f_\xi}{\partial \eta^2}\right) + N_H \frac{\partial E}{\partial \eta} - \frac{f_\xi}{Da} + R\left(\frac{\partial g}{\partial \xi} + \frac{\partial g}{\partial \eta}\right), \quad (44)$$

$$f_\xi \frac{\partial f_\eta}{\partial \xi} + f_\eta \frac{\partial f_\eta}{\partial \eta} = (1+R)\left(\frac{\partial^2 f_\eta}{\partial \xi^2} + \frac{\partial^2 f_\eta}{\partial \eta^2}\right) + N_H \frac{\partial E}{\partial \eta} - \frac{f_\eta}{Da} + R\left(\frac{\partial g}{\partial \xi} + \frac{\partial g}{\partial \eta}\right). \quad (45)$$

Case IV: Purely hydrodynamic micropolar flow in a Darcian porous medium

With $N_H = 0$, and with $Fs \to 0$, then biomagnetic effects and inertial drag effects vanish and the momentum equations now become:

$$f_\xi \frac{\partial f_\xi}{\partial \xi} + f_\eta \frac{\partial f_\xi}{\partial \eta} = (1+R)\left(\frac{\partial^2 f_\xi}{\partial \xi^2} + \frac{\partial^2 f_\xi}{\partial \eta^2}\right) - \frac{f_\xi}{Da} + R\left(\frac{\partial g}{\partial \xi} + \frac{\partial g}{\partial \eta}\right), \quad (46)$$

$$f_\xi \frac{\partial f_\eta}{\partial \xi} + f_\eta \frac{\partial f_\eta}{\partial \eta} = (1+R)\left(\frac{\partial^2 f_\eta}{\partial \xi^2} + \frac{\partial^2 f_\eta}{\partial \eta^2}\right) - \frac{f_\eta}{Da} + R\left(\frac{\partial g}{\partial \xi} + \frac{\partial g}{\partial \eta}\right). \quad (47)$$

The boundary conditions remain unchanged in all four cases, from the conditions given in (17). These four cases can also be modified for the case of Newtonian flow by setting $R \to 0$, which negates the micropolarity effects.

6 Results and discussions

The velocity, microrotation, temperature are computed for the controlling thermophysical parameters namely, the micropolar parameter, R, biomagnetic parameter, N_H, Darcy number, Da, Forcheimmer number, Fs and magnetic field strength, Mn. The geometrical parameters, namely L and l are given nominal values 1.0 m, 0.01 m respectively, following [49, 50]. Eckert number $Ec = 2.476 \times 10^{-6}$ and Prandtl number $Pr = 20$, following [47]. For a magnetic field of 8 Tesla, blood has the following (dimensional) properties: kinematic viscosity $= 3.1 \times 10^{-6}$ m^2/s and density $= 1050$ kg/m^3, for which blood has reached a saturated magnetization of 60 A/m, as described by Haik et al. [50]. A magnetic field of 8 Tesla is very strong but is nominal for the derivation of the Mn parameter. Loukopoulos and Tzirtzilakis [53] have also implemented this value and the validity of the derived Mn values is provided in [53]. A similar approach was used by Tzirtzilakis et al. [54]. We note that this value of 8 Tesla is excessive and there may be practical problems in creating such a magnetic field. However in numerous applications, for example magnetic

drug targeting, magnetic nanoparticles are injected in the blood in order to utilize them as a drug delivery system for localized therapy. Similar nanospheres have been constructed in order to increase the magnetization of blood. These nanospheres attach to the erythrocytes (red blood cells) and as a consequence, the magnetization of blood may be enhanced by one or two orders of magnitude. Thus with the addition of magnetic nanoparticles in blood, it is possible to achieve the same magnetic number, Mn, using a magnetic field of order 1 Tesla. Further details are provided in the studies by Kashan et al. [61] and Haik et al. [62] which analyze stenotic orifice and thrombus biomagnetic Newtonian flows respectively. In actual numerical computations, sensitivity analysis has been performed to establish a good range of N_H and Mn values which illustrate graphically the influence of *varying* such a parameter on velocity and micro-rotation profiles. More exact scenarios using physically accurate data are still under study by the authors and future articles will elaborate more extensively thereof.

Figure 2 illustrates the ξ-direction translational velocity (f_ξ) profile versus dimensionless ξ coordinate for various micropolar parameter R values, with $Da = 1.0$, $Fs = 1.0$ and $N_H = 10^6$ fixed. The flow regime is therefore *micropolar biomagnetic Darcy-Forcheimmer flow*. The case for $R = 0$ corresponds to Newtonian fluid flow where micro-rotational effects vanish. The peak velocity occurs for $R = 0$ and equals 0.001. As micropolar effects increase, R rises (i.e. greater vortex viscosity) and peak velocities are depressed. Hence for a maximum value of R (=4) the lowest f_ξ velocity is observed. For the case of $R = 1$, the profile is shifted to the right; in all other cases it is skewed to the left. The case of $R = 1$ corresponds to when the micropolar vortex viscosity is identical to the fluid dynamic viscosity. In all cases the profiles are bell-shaped and decrease as ξ tends to the end of the range i.e. edge of the square regime. These trends are consistent with other micropolar flow simulations reported in the literature, for example by Gorla et al. [63].

Figure 3 depicts the dimensionless η-direction velocity profiles versus η coordinate for various R values. For all cases ($R = 0, 1, 2, 3, 4$) the profiles rise monotonically and then decrease asymptotically towards the η axis as η tends to the end of the range. As with the f_ξ velocity, the maximum value of f_η is observed for the case of $R = 0$ for which it has a value of 0.18. This peak value is approximately halved to 0.09 for the case of $R = 1$ and to 0.03 for the case of $R = 4$ (strong micropolarity). Clearly as with f_ξ, the f_η values are reduced with increasing R so that increasing micropolarity decelerates the fluid flow.

Figure 4 illustrates the variation of micro-rotation (g) with ξ coordinate with various micropolar parameters (R). In all cases the profiles are positive up to $\xi \sim 0.1$ after which they become negative. The maximum micro-rotation (angular velocity) magnitude corresponds to the case of $R = 0$, for which the flow is Newtonian. With increasing vortex viscosity, the angular velocities are reduced progressively in magnitude, indicating a deceleration in the micro-element spin.

Figure 5 illustrates the profile for dimensionless temperature (θ) versus dimensionless ξ coordinate for different value of R. The flow regime is therefore micropolar biomagnetic Darcy-Forcheimmer flow. The

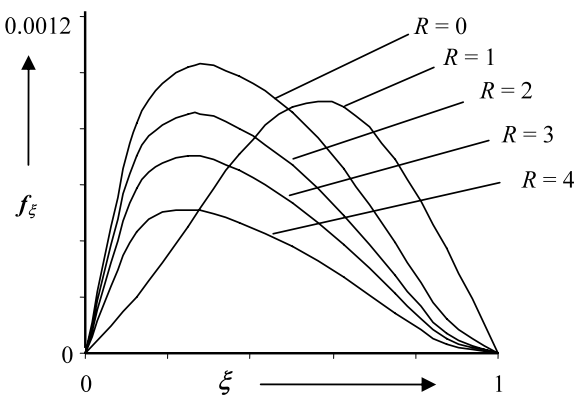

Fig. 2 Velocity (f_ξ) for different R ($N_H = 10^6$, $Fs = 1.0$, $Da = 1.0$)

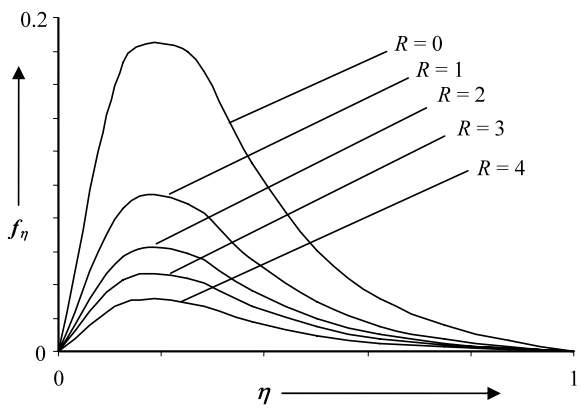

Fig. 3 Velocity (f_η) for different R ($N_H = 10^6$, $Fs = 1.0$, $Da = 1.0$)

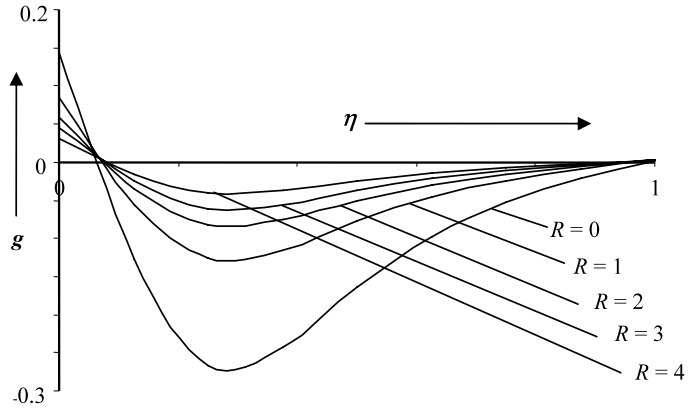

Fig. 4 Microrotation for different R ($N_H = 10^6$, $F_s = 1.0$, $Da = 1.0$)

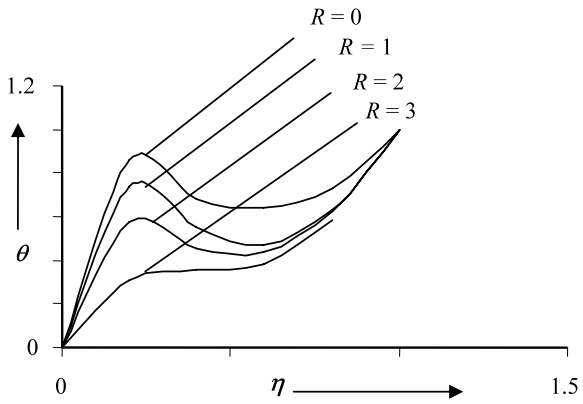

Fig. 5 Temperature for different R ($N_H = 10^6$, $Fs = 1.0$, $Da = 1.0$)

peak velocity occurs for $R = 0$ and equals 0.9. As micropolar effects increase, R rises (i.e. greater vortex viscosity) and peak temperature are depressed. Hence for a maximum value of R, the lowest temperature is observed, indicating that the presence of microconstituents i.e. suspended particles in the micropolar blood, causes cooling of the flow regime.

Figures 6 to 9 show the distribution of f_ξ, f_η, g and θ profiles with ξ for the effects of biomagnetic parameter N_H. In all cases $Da = 1.0$, $Fs = 1.0$ and $R = 1.0$, so that the flow regime is micropolar and non-Darcian. The profiles of f_ξ versus ξ for $N_H = 1000000$ up to 5000000. As discussed earlier, the selected values of the biomagnetic number is important, these are characteristic of blood flow in a magnetic field of flux density of 8 Tesla, following Haik et al. [45], which are in turn based on data derived from Rosensweig [64] concerning ferrohydrodynamic liquids.

Figure 6 indicates that a rise in the value of N_H from 1000000 up to 5000000, depresses the ξ-directional dimensionless translational velocity (f_ξ) with distance along the ξ coordinate. Peak velocity is therefore observed for the lowest value of N_H. The magnetic field dissipates kinetic energy in the micropolar blood and thereby has a retarding effect on the blood flow regime in the square zone. f_ξ values are therefore depressed considerably with increasing N_H values. The location of the magnetic field applied is also significant and as such can be used to control the blood flow in medical devices. A maximum value of f_ξ of 0.005 is computed for $N_H = 1000000$, diminishing to approximately 0.004 for $N_H = 2000000$. All profiles are parabolic and skewed to the left, so that the peak velocities in the ξ-domain are obtained prior to the mid-point of the range. All profiles descend asymptotically to zero as ξ tends to 1.

Figure 7 depicts the f_η distributions with η-coordinate for various N_H values. The profiles are more constricted than in the case of the f_ξ/ξ plots, with peak velocities being attained in the vicinity of $\eta = 0.2$ the maximum velocities correspond again to the weakest biomagnetic field case i.e. $N_H = 1000000$. All profiles descend after peaking to zero at $\eta = 1$. Clearly again therefore N_H induces an impeding effect on the momentum in the η direction, causing a deceleration in the flow.

Dimensionless micro-rotation i.e. angular velocity profiles (g) versus ξ coordinate are illustrated in Fig. 8, for various N_H values. Angular velocity shows a positive trend up to approximately $\xi = 0.1$, after

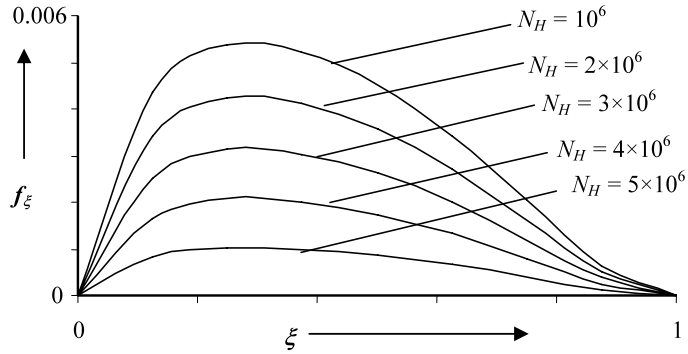

Fig. 6 Velocity (f_ξ) for different N_H ($Da = 1.0$, $Fs = 1.0$, $R = 1.0$)

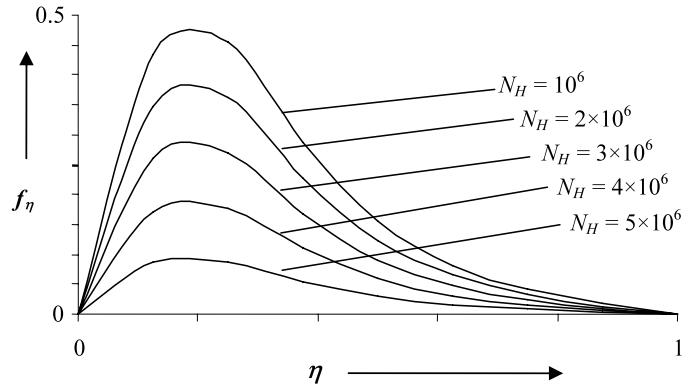

Fig. 7 Velocity (f_η) for different N_H ($Da = 1.0$, $Fs = 1.0$, $R = 1.0$)

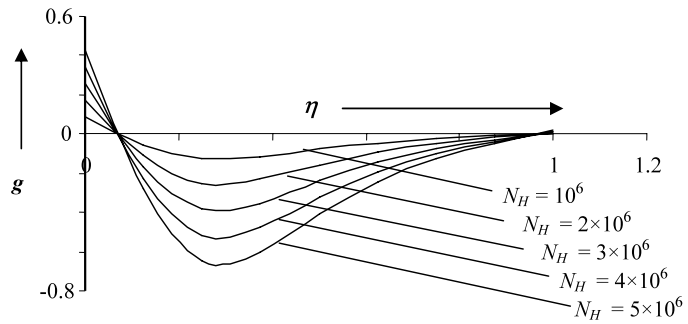

Fig. 8 Microrotation for different N_H ($Da = 1.0$, $Fs = 1.0$, $R = 1.0$)

which values become negative. A reversal in microelement spin occurs at about $\xi \sim 1$, after which $g$values are sustained as negative for the remainder of the ξ range. Maximum magnitudes of g correspond to a maximum N_H value (5000000) and minimum magnitudes to the minimum value of N_H (1000000). Biomagnetic field therefore has a positive effect on the particle spin, which would imply that blood corpuscles (microelements) spin faster in stronger magnetic fields. All profiles tend steadily in a monotonic fashion to zero as $\xi \to 1$.

Figure 9 depicts the θ distributions with ξ-coordinate for various N_H values. The maximum temperature correspond to the weakest biomagnetic field case i.e. $N_H = 1000000$. As N_H increases all profiles are parabolic and skewed to the left, so that the peak ve-

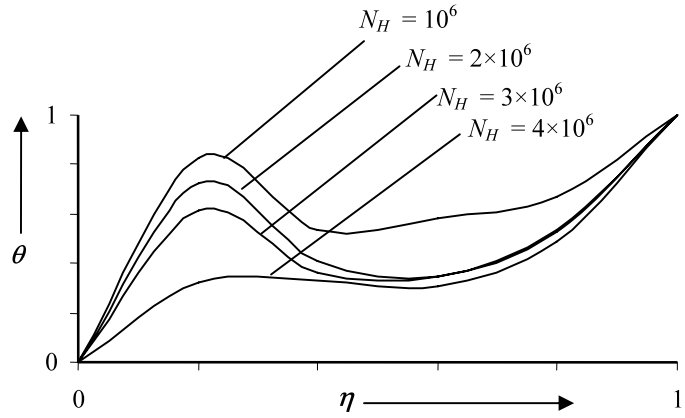

Fig. 9 Temperature for different N_H ($Da = 1.0$, $Fs = 1.0$, $R = 1.0$)

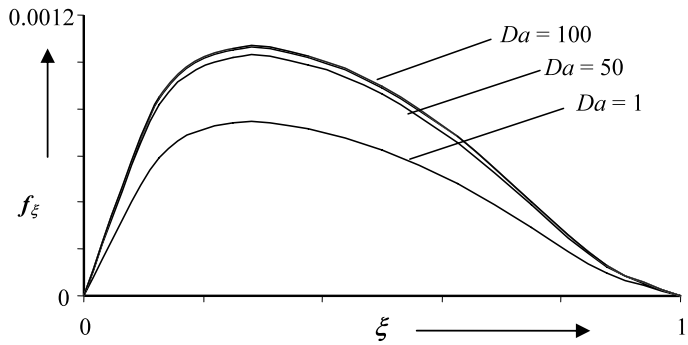

Fig. 10 Velocity (f_ξ) for different Da ($N_H = 10^6$, $R = 1.0$, $Fs = 1.0$)

locities in the ξ-domain are obtained prior to the midpoint of the range.

The effects of porous medium hydrodynamic impedance, embodied in the Darcy number (Da) and the Forcheimmer number (Fs), on the profiles of f_η, g, versus ξ or η coordinate, are illustrated in Figs. 10 to 12 and 13 to 15 respectively.

In Fig. 10 f_ξ distributions versus ξ for $Da = 1$, 50, 100 are obtained. As Da rises from 1 to 100, the regime becomes increasingly porous i.e. more and more fluidic. Bulk solid matrix resistance, i.e. Darcian drag therefore decreases (inverse relationship with Da). The fluid flow therefore accelerates and f_ξ velocities are increased from a peak of 0.0007 (for $Da = 1$) to 0.001 (for $Da = 100$). All profiles rise monotonically from $f_\xi = 0$, peak at $\xi \sim 0.3$, then fall steadily to zero as $\xi \to 1$. The rate of descent of the profiles is less than the rate of ascent, indicating that momentum is boosted in the range $\xi = 0$ to $\xi = 0.3$, but decreases after $\xi = 0.3$.

Figure 11 shows the f_η velocity distribution with η coordinate for $Da = 1, 50, 100$. As for the f_ξ velocity profiles the f_η velocities peak early in the η-domain at $\eta \sim 0.2$. All profiles grow faster prior to $\xi \sim 0.2$, peak and then descend after $\xi \sim 0.2$ tending to zero as $\eta \to 1$. As with the f_ξ velocities, the maximum f_η velocity corresponds to $Da = 100$ ($f_\eta \sim 0.09$) and the minimum f_η velocity occurs for the case of $Da = 1$ ($f_\eta \sim 0.083$); the profile maxima are closer than for the f_ξ velocity plots. $Da = 1$ physically relates to the least porous of the three cases i.e. lowest permeability, corresponding to the maximum matrix resistance of the solid particles in the flow regime. In a biomechanical context these would be generated by the tissue structure through which the blood is flowing. It is observed that there is only a fractional increase in f_η velocity as Da is doubled from 50 to 100, but a much larger rise when it increases by a factor of 50 from 1 to 50.

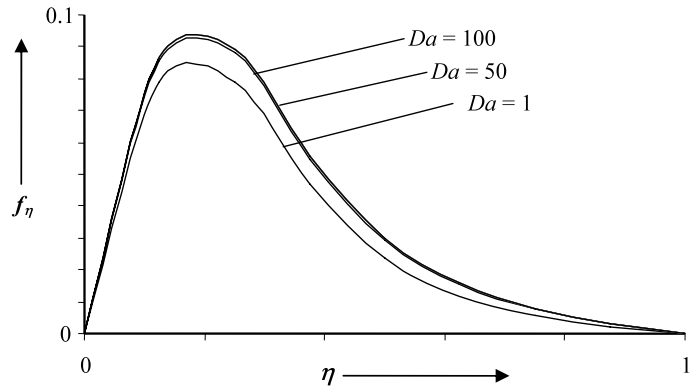

Fig. 11 Velocity (f_η) for different Da ($N_H = 10^6$, $R = 1.0$, $Fs = 1.0$)

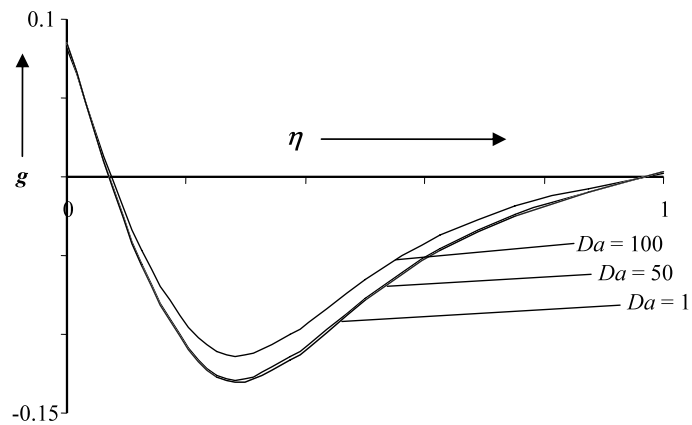

Fig. 12 Microrotation for different Da ($N_H = 10^6$, $R = 1.0$, $Fs = 1.0$)

Figure 12 depicts the variation of g profiles with ξdirection coordinate in the square porous (tissue) regime for $Da = 1$, 50, 100. In this case (as with the other g plots for the case of varying N_H and R) the angular velocities begin positive (all at $g \sim 0.075$) at $\xi = 0$, and then reduce rapidly to zero at $\xi \sim 0.1$ (indicating no spin of the blood corpuscles i.e. microelements) at this location, and then assume negative values for the remainder of the flow regime. The curves all reach a minimum at $\xi \sim 0.03$ and then ascend back to zero at $\xi = 1$. The lowest value of g is observed for $Da = 1$ i.e. the most negative angular velocity. For $Da = 100$, the least negative i.e. most positive value of g is observed. Micro-rotation values therefore also increase i.e. become more positive with a rise in the Darcy number, indicating that for an increasingly fluid regime, the non-deformable blood microelements (corpuscles) spin faster. It would therefore appear that in highly porous tissue zones, blood cells can rotate faster in the flow regime.

The effects of inertial porous drag parameter, Fs, on the f_ξ, f_η, and g profiles are illustrated in Figs. 13 to 15. As with other profiles we have fixed $N_H = 1000000$, and the other parameters to unity (i.e. R, Da). Higher Forcheimer numbers imply greater inertial drag effects so that the flow velocities decrease. In this regime, the Darcian linear drag force effects begin to be dominated by inertial (quadratic) drag effects, so that the creeping (viscous-dominated) flow is swamped out. As Fs is increased from 0.1 to 100, the f_ξ velocity profile (depicted in Fig. 13) clearly decreases substantially from 0.0013 to 0.001. The f_ξ profiles increase sharply from zero at $\xi = 0$ to peak at approximately $\xi = 0.27$, and then decrease smoothly to zero as ξ tends to 1. For higher Fs values the profiles in the vicinity of the peaks are also flatter.

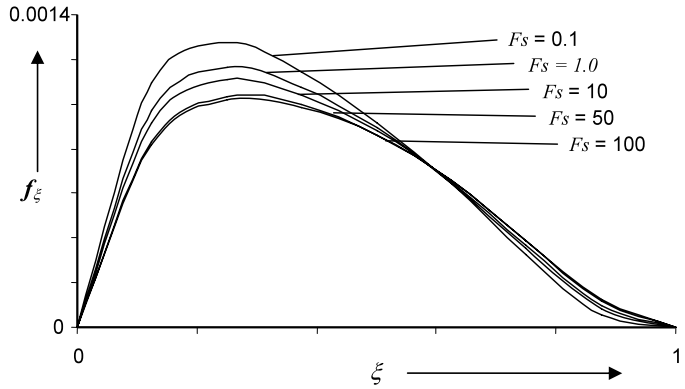

Fig. 13 Velocity (f_ξ) for different Fs ($N_H = 10^6$, $R = 1.0$, $Da = 1.0$)

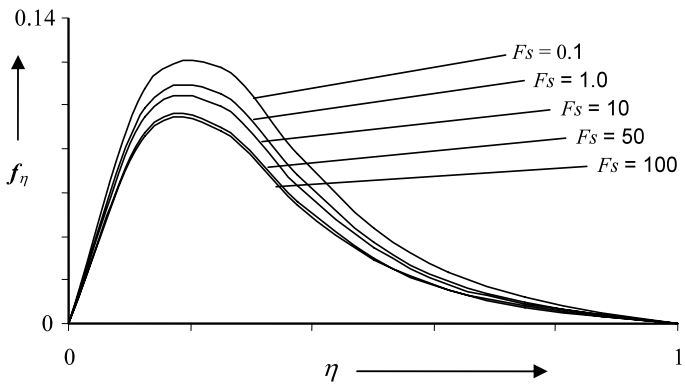

Fig. 14 Velocity (f_η) for different Fs ($N_H = 10^6$, $Da = 1.0$, $R = 1.0$)

Figure 14 shows the f_η velocity distribution with η coordinate for $Fs = 0.1$, 1, 10, 50, 100. Again we see that the minimum f_η velocity corresponds to the maximum Fs value i.e. when inertial effects are most dominant. The peak velocity falls from $f_\eta \sim 0.12$ for $Fs = 0.1$ to $f_\eta \sim 0.095$ for $Fs = 100$. All the curves grow steadily from $f_\eta = 0$ at $\eta = 0$ to a peak at approximately $\eta = 0.2$ and then descend gradually to zero at $\eta = 1$. The rate of ascent of f_η with η up to the peak points is seen to be greater than the rate of descent, as compared with the rate of ascent of f_ξ with ξ, and its subsequent descent rate.

In Fig. 15 the variation of g i.e. angular velocity with ξ direction coordinate in the square porous (tissue) regime for $Fs = 0.1$, 1, 10, 50, 100 is plotted. It is clear that the most positive values of g are associated again with the maximum Fs value ($Fs = 100$) and the most negative g values with $Fs = 0.1$ ($g \sim -0.17$). The least angular velocities therefore correspond to the lowest Fs values, with increasing inertial effects the angular velocities rise i.e. become more positive and tend to zero at $\xi \sim 1$. In all cases g values descend from 0.08 at $\xi = 0$. At $\xi \sim 0.08$ micro-rotations become zero indicating that spin of blood corpuscles i.e. microelements is inhibited at this location. Reverse spin is observed from $\xi \sim 0.08$ for the remainder of the range to $\xi = 1$.

Figure 16 shows the θ distributions versus ξ for different values of $Mn = 315$, 215, 115. As Mn rises, the temperature attains its maximum value at 0.8. The temperature peaks will diminish with the decrement in Mn i.e. they rise with an increase in Mn which is explained by the heating of the fluid by increasing magnetic field intensity, boosting temperatures in the flow regime.

A comparison of the computations with the finite element and finite difference methods has also been conducted for selected values of Mn, Pr, Ec, N_H, R, Da and Fs. Excellent agreement is observed between both methods, as illustrated in Table 1, where the re-

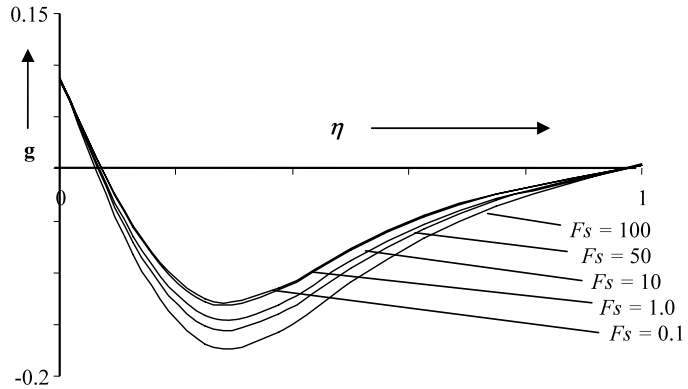

Fig. 15 Microrotation for different Fs ($N_H = 10^6$, $Da = 1.0$, $R = 1.0$)

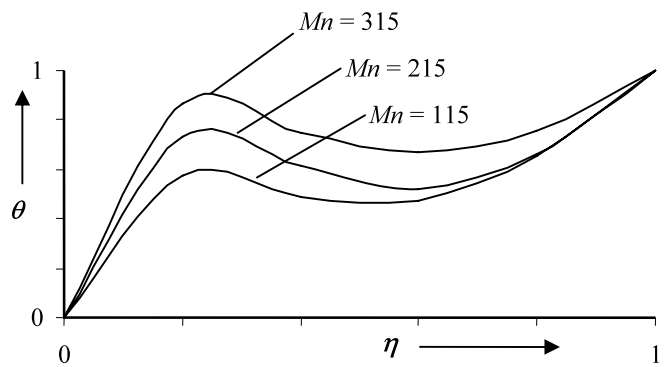

Fig. 16 Temperature for different Mn ($N_H = 10^6$, $Da = 1.0$, $Fs = 1.0$, $R = 1.0$)

Table 1 Comparison of the results (FEM-finite element vs FDM-finite difference)

η	f_ξ		f_η	
	FEM	FDM	FEM	FDM
0	0.000000	0.000000	0.000000	0.000000
0.2	0.020610	0.020654	0.085590	0.085572
0.4	0.011420	0.011438	0.072390	0.072368
0.6	0.003332	0.003359	0.028750	0.028741
0.8	0.000129	0.000176	0.008553	0.008527
1	0.000000	0.000000	0.000000	0.000000

Table 2 Velocity function f_ξ for η direction with different number of elements ($N_H = 10^6$, $R = 1.0$, $Fs = 1.0$)

ξ	No. of elements		
	80	100	120
0.0	0	0	0
0.2	0.05722	0.05720	0.05721
0.4	0.07518	0.07524	0.07522
0.6	0.05891	0.05895	0.05896
0.8	0.02948	0.02952	0.02954
1.0	0	0	0

sults for both methods can be seen to agree up to four decimal places. A comparison of accuracy obtained with three different finite element meshes is also shown in Table 2, where we have computed the variation of the f_ξ translational velocity component with η coordinate for 80, 100 and 120 element scenarios. The results concur up to three decimal places. Additionally we have computed Nusselt numbers for a wide range of parameters which provide a basic idea of the heat transfer rates in the porous tissue medium. These results are however not included here for conservation of space.

7 Conclusions

Computational solutions have been obtained for the two-dimensional, laminar, incompressible, biomagnetic, micropolar blood flow and heat transfer in a two-dimensional Darcian porous medium. The magneto-thermo-hydrodynamic coupling has been simulated by both temperature function and magnetic field intensity function. Appropriate velocity, temperature and micro-rotation boundary conditions have been prescribed at the walls. A number of special cases of the general flow model have been presented which are pertinent in benchmarking the computations with earlier non-biomagnetic and Newtonian studies. Our computations have shown that:

(i) A rise in micropolar vortex viscosity parameter (R) reduces the transformed translational velocity components i.e. f_ξ, f_η implying that increasing micropolarity decelerates the fluid flow.
(ii) Increasing micropolar vortex viscosity parameter (R) decreases the angular velocity (g) i.e. micro-rotation progressively indicating that the biofluid micro-elements rotate slower with greater vortex viscosity.
(iii) Increasing micropolar vortex viscosity parameter (R) induces a decrease in peak temperature values (θ) indicating that increasing micropolarity cools the blood flow.
(iv) Increasing biomagnetic number (N_H) causes a decrease in the ξ-directional dimensionless translational velocity (f_ξ) with distance along the ξ coordinate i.e. flow is decelerated by rising N_H.
(v) Increasing biomagnetic number (N_H) generally induces a fall in f_η values with η-coordinate i.e. again causes a deceleration in the flow.
(vi) Increasing biomagnetic number (N_H) boosts the micro-rotation (g) values.
(vii) Increasing biomagnetic number (N_H) reduces the temperatures (θ) in the flow domain.
(viii) Increasing Darcy number (Da) increases f_ξ velocity plotted against ξ implying an acceleration in the flow as the regime becomes increasingly permeable.
(ix) Increasing Darcy number (Da) boosts f_ξ velocity versus η again indicating that the flow is accelerated as the regime becomes increasingly permeable.
(x) Increasing the Darcy number, Da substantially increases the micro-rotation (g) in the porous domain.
(xi) An increase in Forchheimer inertial number (Fs) decreases the f_ξ velocity values indicating that flow is decelerated.
(xii) An increase in Forchheimer inertial number (Fs) decreases the f_η velocity values again implying that flow is decelerated; however the effects are less dramatic than in the case of the f_ξ velocity components.
(xiii) An increase in Forchheimer inertial number (Fs) increases the angular velocity (micro-rotation) values (g).
(xiv) An increase in the magnetic field intensity parameter (Mn) considerably increases temperature (θ) values with η distance throughout the porous domain.

The study reported here constitutes a steady state flow regime. An important extension is therefore to consider transient effects. Additionally the porous medium model can be further refined to represent more accurately-defined geometries encountered in actual biomechanical situations and efforts in this direction are underway.

References

1. Pennes HH (1948) Analysis of tissue and arterial blood temperatures in the resting human forearm. J Appl Physiol 1(2):93–122
2. Charny CK (1992) Mathematical models of bioheat transfer. Bioengineering Heat Transfer, Special Issue, Adv Heat Transf 22:19–155
3. Rubinsky B (1999) Heat transfer in biomedical engineering and biotechnology. In: Proceedings of the 5th ASME/JSME joint thermal engineering conference, AJTE-6528
4. Charm S, Paltiel B, Kurland GS (1968) Heat transfer coefficients in blood flow. Biorheology 5:133–145
5. Victor SA, Shah VL (1975) Heat transfer to blood flowing in a tube. Biorheology 12:361–368
6. Victor SA, Shah VL (1976) Steady state heat transfer to blood flowing in the entrance region of a tube. Int J Heat Mass Transf 19:777–783
7. Chato JC (1980) Heat transfer to blood vessels. ASME J Biomech Eng 102:110–118
8. Lagendijk JJW (1982) The influence of blood flow in large vessels on the temperature distribution in hyperthermia. Phys Med Biol 27:17–23
9. Bég OA, Sajid A (2002) CFD modeling of axisymmetric hemodynamics and heat transfer using ADINA. Technical Report, Biomechanics-III, Universidyne Research Consultancy, Bradford University Science Park, Listerhills, Bradford, UK, November 2002

10. Craciiunescu OI, Clegg ST (1997) Perturbations of large vessels on induced temperature distributions, part A: three-dimensional simulation study. Adv Heat Mass Transf Biotechnol 355:193–198
11. Craciiunescu OI (1998) Influence of blood vessel networks on hyperthermia-induced temperature distributions. PhD thesis, Mechanical Engineering and Materials Science, Duke University, North Carolina, USA
12. Kolios MC, Sherar MD, Hunt JW (2003) Large blood vessel cooling in heated tissues: a numerical study. Phys Med Biol 48:4125–4134
13. Chakravarty S, Sen S (2005) Dynamic response of heat and mass transfer in blood flow through stenosed bifurcated arteries. Korean–Australia J 17(2):47–62
14. Baish JW (1990) Heat transport by countercurrent blood vessels in the presence of an arbitrary pressure gradient. ASME J Biomech Eng 112:207
15. Deng ZS, Liu J (2001) Blood perfusion-based model for characterizing the temperature fluctuations in living tissue. Physica A: Stat Mech Appl 300:521–530
16. Craciiunescu OI, Clegg ST (2001) Pulsatile blood flow effects on temperature distribution and heat transfer in rigid vessels. ASME J Biomech Eng 123(5):500–505
17. Consiglieri L, Santos I, Haemmerich D (2003) Theoretical analysis of the heat convection coefficient in large vessels and the significance for thermal ablative therapies. Phys Med Biol 48:4125–4134
18. Davalos RV, Rubinsky B, Mir LM (2003) Theoretical analysis of the thermal effects during in vivo tissue electroporation. Bioelectrochem J 61:99–107
19. Shrivastava D, McKay B, Romer RB (2005) An analytical study of heat transfer in finite tissue with two blood vessels and uniform Dirichlet boundary conditions. ASME J Heat Transf 127(2):179–188
20. Gafiychuk VV, Lubashevsky IA, Datsko BY (2005) Fast heat propagation in living tissue caused by branching artery network. Phys Rev E 72:051920
21. Cokelet GR (1972) The rheology of human blood. In: Fung YC (ed) Biomechanics-its foundations and objectives. Prentice Hall, New York
22. Skalak R, Chien S (1982) Rheology of blood cells as soft tissues. Biorheology 19:453–461
23. Secomb TW, Chien S, Jan KM, Skalak R (1983) The bulk rheology of close-packed red blood cells in shear flow. Biorheology 20(3):295–309
24. Rodkiewicz SP, Kennedy JS (1990) On the application of a constitutive equation for whole human blood. ASME J Biomech Eng 112:199–206
25. Quemada D (1993) A non-linear Maxwell model of biofluids: application to normal blood. Biorheol J 30:253–265
26. Srivastava VP (2003) Flow of a couple stress fluid representing blood through stenotic vessels with a peripheral layer. Indian J Pure Appl Math 34(12):1727–1740
27. Anand M, Rajagopal KR (2004) A shear-thinning viscoelastic fluid model for describing the flow of blood. Int J Cardiovasc Med Sci 4(2):59–68
28. Choi HW, Barakat AI (2005) Numerical study of the impact of non-Newtonian blood behavior on flow over a two-dimensional backward facing step. Biorheol J 42(6):493–509
29. Eringen AC (1966) Theory of micropolar fluids. USSR J Math Mech 16(1):909–923
30. Ariman T, Turk NA, Sylvester ND (1974) On steady pulsatile flow of blood. ASME J Appl Mech 41:1–7
31. Eringen AC, Kang CK (1976) The effect of microstructure on the rheological properties of blood. Bull Math Biol 38(2):135–159
32. Riha P (1977) Poiseuille flow of microthermopolar fluids. Acta Tech CSAV 22(5):602–613
33. Chaturani P, Mahajan SP (1982) Poiseuille flow of micropolar fluid with non-zero couple stress at boundary with applications to blood flow. Biorheol J 19(4):507–518
34. Hogan HA, Henriksen M (1989) An evaluation of a micropolar model for blood flow through an idealized stenosis. J Biomech 22(3):211–218
35. Muthu P, Kumar BVR, Chandra P (2003) Effect of elastic wall motion on oscillatory flow of micropolar fluid in an annular tube. Arch Appl Mech (Ing Arch) 73(7):481–494
36. Atefi Gh, Moosaie A (2005) Analysis of blood flow through arteries using the theory of micropolar fluids. In: Proceedings of the 12th Iranian biomedical engineering conference, Tabriz, Iran, November 2005
37. Cimpean DS, Pop I, Ingham DB (2006) A problem of steady micropolar flow in a sinusoidal channel. In: SCRA 2006-FIM XIII—thirteenth international conference of the forum for interdisciplinary mathematics on interdisciplinary mathematical and statistical techniques, New University of Lisbon-Tomar Polytechnic Institute, Lisbon-Tomar, Portugal, 1–4 September 2006
38. Sorek S, Sideman S (1986) A porous medium approach for modelling heart mechanics, B l-D case. Math Biosci 81:14–32
39. Preziosi L, Farina A (2002) On Darcy's law for growing porous media. Int J Non-Linear Mech 37:485–491
40. Vankan WJ, Huyghe JM, Janssen JD, Huson A, Hacking WJG, Schrenner W (1997) Finite element analysis of blood flow through biological tissue. Int J Eng Sci 35:375–385
41. Axtell NK, Moongyu P, Cushman JH (2005) Micromorphic fluid in an elastic porous body: blood flow in tissues with microcirculation. Int J Multiscale Comput Eng 3:1
42. Takeuchi T, Mizuno T, Higashi T, Yamagishi A, Date M (1995) Orientation of red blood cells in high magnetic field. J Magn Magn Mater 140:1462–1463
43. Sud VK, Sekhon GS, Mishra RK (1977) Pumping action on blood by a magnetic field. Bull Math Biol 39:385–390
44. Wagh DK, Wagh SD (1992) Blood flow considered as magnetic fluid flow. In: Proceedings of physiological fluid dynamics, pp 311–315
45. Haik Y, Chen JC, Pai VM (1996) Development of biomagnetic fluid dynamics. In: Winoto SH et al (eds) Proceedings of the IX international symposium on transport phenomena in thermal fluids engineering, Singapore, Pacific Centre in Thermal Fluids Engineering, Hawaii USA, June 1996, pp 25–28
46. Sud VK, Sekhon GS (2003) Blood flow through the human arterial system in the presence of a steady magnetic field. Biophys J 84:2638–2645
47. Tzirtzilakis EE, Tanoudis GB (2003) Numerical study of biomagnetic fluid flow over a stretching sheet with heat transfer. Int J Numer Methods Heat Fluid Flow 13(7):830–848
48. Louckopoulos VC, Tzirtzilakis EE (2004) Biomagnetic channel flow in spatially varying magnetic field. Int J Eng Sci 42:571–590

49. Bhargava R, Rawat S, Takhar HS, Bég OA (2006) Finite element solutions for biomagnetic micropolar blood flow in a fluid-saturated non-Darcian porous highly-perfused tissue model. In: 5th world congress in biomechanics, Munich, Germany, July 2006
50. Haik Y, Pai V, Chen CJ (1999) Biomagnetic fluid dynamics. In: Shyy W, Narayanan R (eds) Fluid dynamics at interfaces. Cambridge University Press, Cambridge, pp 439–452
51. Tzirtzilakis EE (1999) A mathematical model for blood flow in magnetic field. Phys Fluids 17:077103
52. Matsuki H, Yamasawa K, Murakami K (1977) Experimental considerations on a new automatic cooling device using temperature sensitive magnetic fluid. IEEE Trans Magn 13(5):1143–1145
53. Loukopoulos VC, Tzirtzilakis EE (2005) Biofluid flow in a channel under the action of a uniform localized magnetic field. Comput Mech 36(5):360–374
54. Tzirtzilakis EE, Xenos M, Lockopoulos VC, Kafoussias NG (2006) Turbulent biomagnetic fluid flow in a rectangular channel under the action of a localized magnetic field. Int J Eng Sci 44:1205–1224
55. Ahmadi G (1976) Self-similar solution of incompressible micropolar boundary layer flow over a semi-infinite plate. Int J Eng Sci 14:639–646
56. Dey J, Nath G (1983) Incompressible micropolar fluid flow over a semi-infinite plate. Int J Eng Sci 21(8):967–972
57. Reddy JN (1985) An introduction to the finite element method. MacGraw-Hill, New York
58. Takhar HS, Agarwal RS, Bhargava R, Jain S (1998) Mixed convective non-steady 3-dimensional micropolar fluid flow at a stagnation point. Heat Mass Transf J 33:443–448
59. Bhargava R, Kumar L, Takhar HS (2003) Finite element solution of mixed convection micropolar flow driven by a porous stretching sheet. Int J Eng Sci 41:2161–2178
60. Bég OA, Takhar HS, Bhargava R, Rawat S, Bég TA (2007) Finite element modeling of laminar flow of a third grade fluid in a Darcy–Forchheimer porous medium with suction effects. Int J Appl Mech Eng 12(1):215–233
61. Khashan SA, Haik Y (2006) Numerical simulation of biomagnetic flow downstream an eccentric stenotic orifice. Phys Fluids 18:11
62. Haik Y, Chen CJ, Chatterjee J (2002) Numerical simulation of biomagnetic fluid in a channel with thrombus. J Vis 5(2):187–195
63. Gorla RSR, Takhar HS, Slaouti A (1998) Magnetohydromagnetic free convection boundary layer flow of a thermal micropolar fluid over a vertical plate. Int J Eng Sci 36:315–327
64. Rosensweig R (1985) Ferrohydrodynamics. MacGraw-Hill, New York